Carbon 121 (2017) 35–47

Contents lists available at ScienceDirect

Carbon

journal homepage: www.elsevier.com/locate/carbon

Thermal conductivity and annealing effect on structure of lignin-based microscale carbon fibers

Jing Liu [1], Wangda Qu [1], Yangsu Xie, Bowen Zhu, Tianyu Wang, Xianglan Bai**, Xinwei Wang*

Department of Mechanical Engineering, 2010 Black Engineering Building, Iowa State University, Ames, IA 50011, USA

ARTICLE INFO

Article history:
Received 19 February 2017
Received in revised form
9 May 2017
Accepted 10 May 2017
Available online 20 May 2017

ABSTRACT

This work reports on systematic investigation of the structure and thermal conductivity of lignin-based carbon fibers (CF) at the microscale. The lignin-based CF is produced by melt-spinning pyrolytic lignin derived from red oak. The 0 K-limit phonon scattering mean free path uncovers a characteristic structure size of ~1.2 nm, which agrees well with the crystallite size by X-ray scattering (0.9 and 1.3 nm) and the cluster size by Raman spectroscopy (2.31 nm). The thermal conductivity of as-prepared CFs is determined at ~1.83 W/m·K at room temperature. The thermal reffusivity of CFs shows little change from room temperature down to 10 K, uncovering the existence of extensive defects and grain boundaries which dominate phonon scattering. The localized thermal conductivity of CFs is increased by more than ten-fold after being annealed at ~2800 K, to a level of 24 W/m·K. Our microscale Raman scanning from less annealed to highly annealed regions shows one-fold increase of the cluster size: from 1.83 nm to 4 nm. This directly confirms structure improvement by annealing. The inverse of the thermal conductivity is found linearly proportional to the annealing temperature in the range of 1000–2800 K.

© 2017 Elsevier Ltd. All rights reserved.

1. Introduction

Over the past few decades, researchers and industries are pursuing high-performance yet lightweight materials in engineering. One of the promising materials is carbon fiber (CF) [1]. The composites using CFs as the reinforced material have high strength, high modulus, high stiffness yet low density (1.75–2.0 g/cm^3) [2]. The tensile modulus of CF ranges from 291 GPa for polyacrylonitrile (PAN) based CF to 940 GPa for ultrahigh modulus pitch-based CF. The typical tensile strength falls in the range of 2.47–5.69 GPa for PAN-based CF [2]. With the excellent mechanical properties, the CFs could be used in reducing the vehicles' total weight and thus to improve the fuel efficiency of vehicles [3]. Apart from this, CF also has potential applications in aerospace structures, sport equipment, turbine blades and so on [4]. Currently, the dominant precursor for producing CFs is polyacrylonitrile [2,4–6], which is a petroleum-based polymer. Despite its unique properties, the application of CF is limited to specific fields mainly due to its high market price related to the cost of PAN, which accounts for 51% of the total production cost of CF [1]. The release of toxic gas during the processing of PAN-based CF is also an environmental concern. Thus, producing low-cost carbon fibers from alternative precursors has been of great interest to many researchers. Lignin has drawn the most attention as an alternative precursor because of its abundance, low cost and relative high carbon content [7]. Lignin is the second abundant biopolymer in nature, accounting for 10–35% of lignocellulosic biomass [8]. Isolated lignin is also available as a by-product from paper industry and bio-refineries. The estimated cost of lignin precursor could be 50–70% lower than the textile grade PAN [9]. Although economically advantageous, lignin-based CFs usually have much lower mechanical properties in comparison to PAN-based CFs mainly due to the lack of the molecular orientation in lignin polymer [10]. On the other hand, CFs produced from mixture of PAN and lignin could have lower cost than PAN-based CFs, while showing good compressive strength [4,11].

In previous studies, research focus has been mostly on the manufacturing of lignin-based CFs and process optimization for improved mechanical properties [12–14]. However, it is also important to note that lignin-based CFs could also be applied as functional materials for other applications where material

* Corresponding author.
** Corresponding author.
E-mail addresses: bxl9801@iastate.edu (X. Bai), xwang3@iastate.edu (X. Wang).
[1] These authors contributed equally to the work.

http://dx.doi.org/10.1016/j.carbon.2017.05.066
0008-6223/© 2017 Elsevier Ltd. All rights reserved.

mechanical properties are not essential [15]. Past work about the relevant thermal properties was focused on carbon nanofibers (CNFs) and PAN-based CFs. Mayhew et al. reported that the *k* of commercially-available CNFs obtained by chemical vapor deposition is 4.6 W/m·K by using T-type probe experimental configuration [16]. The thermal conductivity for PAN-based CFs without extremely high temperature treatment is in the order of tens of W/m·K [6,17]. High temperature (as high as ~3000 °C) treatment is a common method used in lab and industry to improve the microstructure and thermal conductivity of CFs. The *k* of CNFs could be increased by around 40 times after being annealed at 2800 °C for 20 hours [16]. The *k* of high temperature treated PAN-based CFs could be as high as several hundreds of W/m·K [6]. However, so far, seldom work has been reported about the *k* of lignin-based CFs. Recently, we have produced lignin-based CFs by melt-spinning red oak derived pyrolytic lignin. Although still lower than that of PAN-based CFs, the mechanical properties of our lignin-based CFs were at the top range of previously reported lignin-based CFs [18]. In the present study, lignin-based CFs were further tested to examine their thermal properties. Our goal is to study the thermal properties of lignin-based CFs, as well as the structure effect on phonon scattering and thermal transport. Furthermore, through annealing, it is found that the *k* of the lignin-based CFs is expected to increase by ten folds. The *k* of high temperature treated lignin-based CFs could reach tens of W/m·K. One natural question is: To what extent the microstructure of the lignin-based CFs could be improved by the annealing method? We will answer this question through the structure and thermal properties study for the high temperature treated lignin-based CFs.

This work is organized as follows. In the first section, the preparation and processing of lignin-based CFs are introduced. Next, structure studies by Raman, X-ray diffraction (XRD) and X-ray photoelectron spectroscopy (XPS) are presented. In the third part, we show the experimental setup for thermal properties measurement and the corresponding thermal properties study. This is followed by the study of phonon scattering in the lignin-based CFs. Finally, annealing treatment and improvement of the structure and thermal properties are discussed. We will use CF to indicate the lignin-based CF tested in this work.

2. Structural properties of the fiber specimens

2.1. Carbon fiber manufacturing

The carbon fiber specimens used in this study were manufactured from red oak-derived pyrolytic lignin using the melt-spinning method [18]. The production method of pyrolytic lignin and manufacturing process of the lignin-based CFs are shown in Fig. 1(a). Detailed information can be found in our previous study [18]. Briefly, red oak was pyrolyzed in a fluidized bed reactor with a staged-fractionation condenser system. Pyrolytic lignin was isolated from heavy fraction of bio-oil [19]. Because pyrolytic lignin is partly decomposed lignin which has low viscosity upon heating, it was thermally repolymerized to increase its viscosity, making it a suitable precursor for melt-spinning [18]. The as-spun fiber was then subjected to oxidative stabilization at a rate of 0.3 °C/min up to 280 °C, and further carbonized at 3 °C/min up to 1000 °C under argon environment. The produced CFs have diameters varying from 29 to 50 μm, with majority has a diameter between 35 and 40 μm. Further characterizations of the CF are provided in Table 1 and Fig. 1.

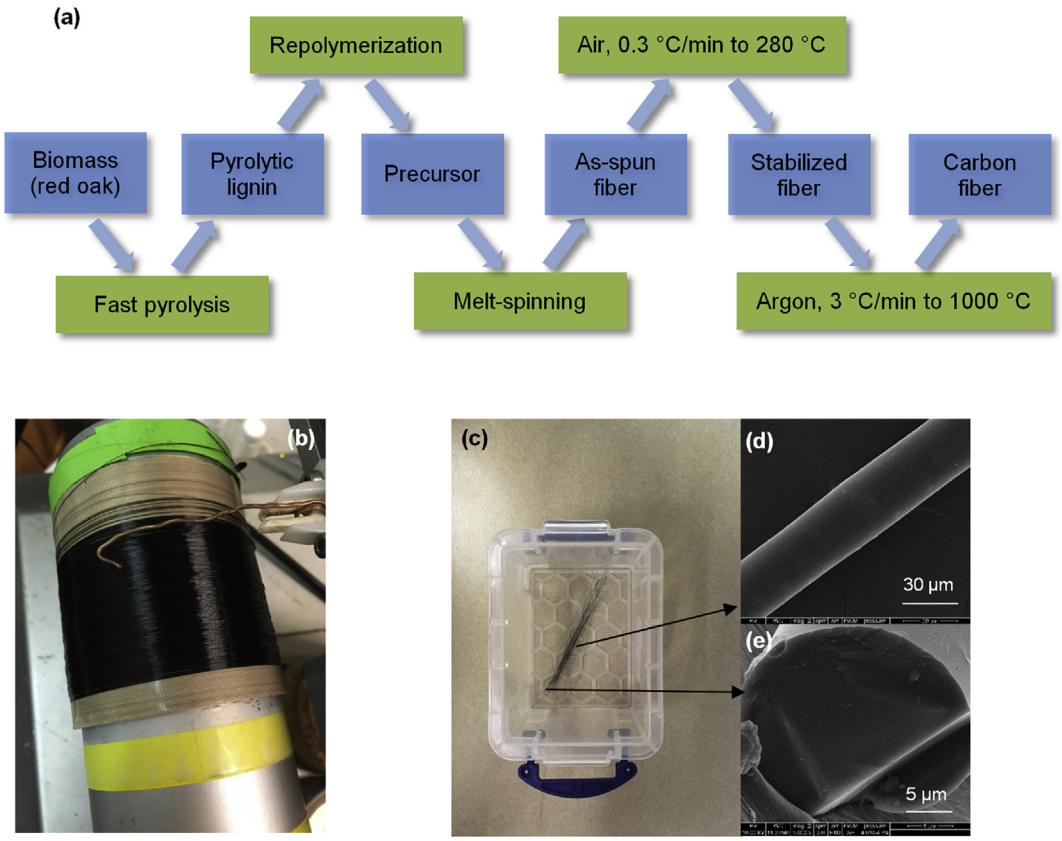

Fig. 1. **(a)** Production of pyrolytic lignin and manufacturing process for the CFs. **(b)** As-spun fiber. **(c)** Carbonized CFs. **(d)** Scanning electron micrograph (SEM) of the surface for a single CF. **(e)** Cross-sectional view of the CF. (A colour version of this figure can be viewed online.)

Table 1
Properties of lignin-based carbon fibers [18].

	Lignin-based CFs
Diameter (μm)	29–50
Tensile strength (MPa)	855 ± 159
Modulus (GPa)	85 ± 37
Strain (%)	1.01 ± 0.3
Carbon content (%)	93.4
Hydrogen content (%)	0.74
Oxygen content (%)	4.55

2.2. Structural characterization of the lignin-based carbon fibers

Before characterizing the thermal properties, the microstructure and elemental composition of the CFs are studied by Raman, XRD and XPS. The Raman spectrum [Fig. 2(a), E_{Laser} = 2.33 eV (532 nm)] of the CFs exhibits two wide and overlapping peaks at 1350 and 1580 cm^{-1}, corresponding to *D* peak and *G* peak in the CFs. A flat 2*D* region is also observed. This is a typical Raman spectrum of graphite oxide (GO) [20]. The *D* and *G* peaks' full width at high maximum (FWHM) are broadened due to structure disorder [21]. It is known that *D* peak is assigned to the breathing mode of A_{1g} as disorder exists. Its intensity (I_D) could be used to show the degree of disorder in the structure. *G* peak results from the motion of sp^2-hybridized carbon stretching mode and its intensity reflects the degree of carbonization [22]. The Lorenz function is employed to fit the *D* and *G* peaks, respectively, which are shown in red and blue lines in the inset of Fig. 2(a). Using the ratio of peak intensities I_D/I_G, the degree of disorder in the CFs is characterized. It has been proposed that I_D/I_G could be interpreted with an empirical formula: $I_D/I_G = C(\lambda)/L_a$, which is called the TK equation to name after Tuinstra and Koenig [22,23]. Here, $C(\lambda) = (2.4 \times 10^{-10}\ nm^{-3}) \times \lambda^4$, λ is the wavelength (unit: nm) of the excitation laser, which is 532 nm in this research. L_a is cluster size [22,23]. In this work, Raman spectrum of multiple points is obtained, and I_D/I_G ranges from 2.18 to 2.42. The average L_a for the CFs is then estimated to be 2.31 nm.

Fig. 2(b) shows the XRD results (XRD, Siemens D500 X-ray diffractometer using a Cu X-ray tube) of the CFs. Two broad peaks are observed at 23.53° and 43.18°, corresponding to (002) peak and (100) peak. The corresponding lattice spacing is determined to be 0.378 and 0.209 nm for (002) and (100) peak, respectively. For graphite oxide (GO), the lattice spacing between carbon layers (d_{002}) is 0.65–0.75 nm, depending on the functional group content in GO [24]. For PAN-based CFs, d_{002} varies from 0.3395 nm to

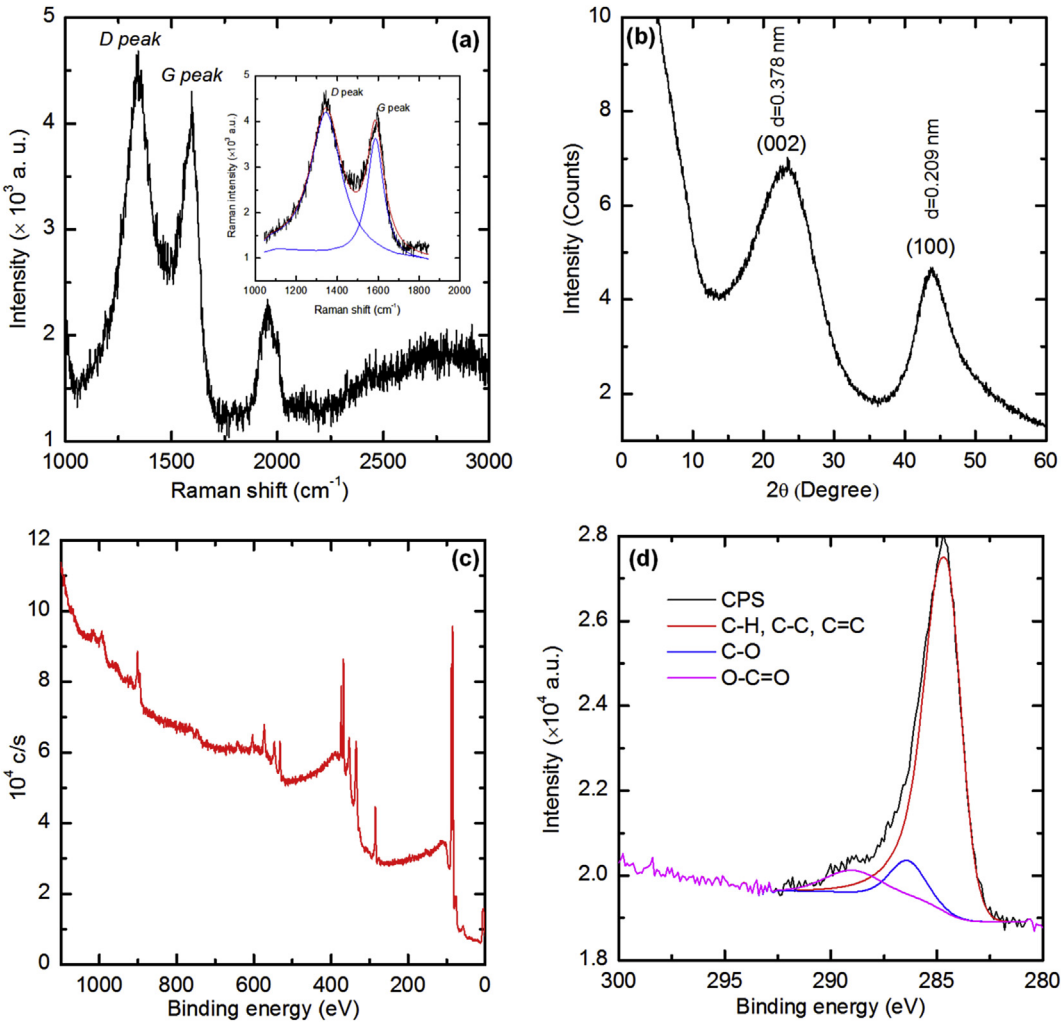

Fig. 2. **(a)** Raman spectrum. Broad *D* peak at 1350 cm^{-1} and *G* peak at 1580 cm^{-1} are observed. No sharp 2*D* peak is observed. Lorentz function is employed to fit the *D* and *G* peak, as shown in red and blue lines in the inset. **(b)** XRD diffractogram. **(c)** X-ray photoelectron spectra of CFs. **(d)** The XPS C1s spectrum, indicating different bonds for carbon atoms in the sample surface. (A colour version of this figure can be viewed online.)

0.353 nm [6]. We speculate that the existence of GO in our sample leads to a larger lattice spacing between carbon layers than that of PAN-based CFs. The XRD also indicates the low crystallinity of the CFs. The crystallite size L_c along the *c*-axis is obtained from the (002) peak, and it is determined to be 0.9 nm. L_c along the basal plane is 1.3 nm obtained by the (100) peak. There is discrepancy between the L_a determined by Raman (2.31 nm) and L_c determined by XRD. This is due to different mechanisms in determining the cluster size: L_a determined by Raman reflects the phonon scattering mean free path of optical phonons, while L_c determined by XRD reflects the real crystallite size.

Chemical analysis of the CFs is conducted by XPS on a PHI55000 XPS with an Al Kα X-rays (1486.6 eV). The binding energy ranges from −5 to 1100 eV with a step 0.5 eV, and the pass energy is 153.6 eV. Fig. 2(c) shows the X-ray photoelectron spectra of the CFs. The elemental composition is determined as: C (93.4%), H (0.74%) and O (4.55%). The C1s XPS spectrum is shown in Fig. 2(d). It has three obvious peaks by deconvolution, corresponding to C—H, C—C, C═C (these three totally 84.83%) and C—O (7.87%) and O—C═O (7.29%), respectively. The existence of these functional groups also leads to a larger lattice spacing between carbon layers than that of PAN-based CFs. The large lattice spacing is not favorable for heat conduction, mainly because of the induced loose contact between lattice layers. The higher degree of disorder usually accompanies smaller crystallite size, larger carbon layer lattice spacing and poor crystal orientation, which finally leads to a lower thermal conductivity [6,25,26].

3. Experimental details for thermal transport characterization

3.1. Thermal characterization principle

The thermal diffusivity of the CFs from room temperature (RT) down to 10 K is measured by the cryogenic transient electrothermal (TET) technique. As shown in Fig. 3(a), the to-be-measured sample is suspended between two electrodes. The contacts between the sample and the two electrodes are secured by silver paste. In this way, the thermal contact resistance could be reduced to a negligible level. Then the whole sample is placed in a vacuum chamber, whose environmental temperature from RT to 10 K is offered by a Janis closed cycle refrigerator (CCR) system. During the thermal measurement, the vacuum level remains under 0.5 mTorr by a liquid nitrogen cold-trapped mechanical vacuum pump. It helps eliminate the heat convection effect in the measurement. When doing the TET test, a small step current is applied to the sample to induce joule heating by a current source (Keithley 6221). The temperature rise caused by the joule heating results in a decrease of the sample resistance, and thus the voltage over the fiber will has a decreasing profile. The voltage evolution over the fiber is monitored by an oscilloscope (Tektronix DPO3052). With known voltage evolution, the normalized temperature (ΔT^*) evolution is obtained as $[V(t)-V_0]/[V(t\rightarrow\infty)-V_0]$. This value could be used in the fitting to determine the thermal diffusivity. Here, V_0 and $V(t\rightarrow\infty)$ are the initial voltage and steady state voltage over the sample. More details could be found in our previous work [27].

The heat conduction in the CF could be regarded as 1-D thermal transport due to the sample's high aspect ratio (length to diameter). Thus, the governing equation could be described as:

$$\frac{\partial(\rho c_p T)}{\partial t} = k\frac{\partial^2 T}{\partial x^2} + \dot{q} - \frac{4\varepsilon\sigma(T^4 - T_0^4)}{d}, \tag{1}$$

where ρ, c_p and k are the density, specific heat and thermal conductivity of the sample, respectively. d is the sample's average diameter. $\dot{q}$ is the joule heating power per unit volume. It has the form of I^2R_s/AL. Here, A and L are the cross-sectional area and length of the sample. I and R_s are the fed-in current and the resistance of the sample, respectively. $4\varepsilon\sigma(T^4-T_0^4)/d$ describes the effect of radiation. Since the aluminum electrodes are much larger than the sample dimension, the temperature of the electrodes could be regarded unchanged when a small current goes through it. The boundary condition for this heat transport can be described as $T = T_0$. The normalized temperature rise is solved as:

$$\Delta T^* = \frac{96}{\pi^4}\sum_{m=1}^{\infty}\frac{1-\exp[-(2m-1)^2\pi^2\alpha_{eff}t/L^2]}{(2m-1)^4}. \tag{2}$$

Here, α_{eff} is the effective thermal diffusivity includes the radiation effect [detailed in Eq. (3)]. Using different trial values of α_{eff}, the experimentally obtained normalized temperature rise could be fitted with the theoretical equation. The value giving the least square difference is taken as the effective thermal diffusivity. Additionally, the thermal diffusivity could be directly determined by the characteristic point of the ΔT^*~t curve. From Eq. (2), the characteristic point is obtained when ΔT^* is 0.8665. Details could be found in Ref. [28]. The effective thermal diffusivity could be written as a function of characteristic time (τ_c) as: $\alpha_{eff} = 0.2026L^2/\tau_c$. This could be applied in the quick analysis of effective thermal diffusivity in addition to global fitting.

The effective thermal diffusivity includes the real thermal diffusivity (α_{real}) and effect of radiation (α_{rad}). It can be expressed as:

$$\alpha_{eff} = \alpha_{real} + \frac{1}{\rho c_p}\frac{16\varepsilon\sigma T^3}{\pi^2}\frac{L^2}{d}, \tag{3}$$

where ε (=0.85) [29] and σ (=5.67 × 10^{-8} W/m^{2}K^4) are the emissivity and Stefan-Boltzmann constant, respectively. T is the temperature of the sample during the experiment. The TET technique has been proven to be a valid and reliable method to measure the thermal diffusivity of various samples. For instance, in Ref. [28] the thermal diffusivity of Pt wire determined by TET technique (2.53 × 10^{-5}–2.78 × 10^{-5} m^2/s) agreed well with that (2.51 × 10^{-5} m^2/s) from other references [30]. Using the TET technique, the thermal diffusivity of microscale polyacrylonitrile fiber was measured to be 1.77 × 10^{-7} m^2/s, agreeing well with that of bulk polyacrylonitrile (1.76 × 10^{-7} m^2/s) [31].

3.2. Experimental details for the thermal properties characterization of lignin-based CF

In this work, the density of the sample is obtained by measuring the weight and volume of CFs. Using an analytical balance (Radwag xA 82/220/2x), the weight of the to-be-measured CFs is 0.13 mg. The average diameter and the length of the to-be-measured sample is 40.0 μm and 47.27 mm, respectively. Thus, the density of the CFs is determined to be 2.189 g/cm^3. The specific heat capacity value at RT is set as 709 J/g·K, which is corresponding to the specific heat value of graphite from literature [32]. In the thermal properties measurement, three samples (S1, S2 and S3) are used to do the cryogenic TET tests for structure domain size study. TET characterizations are conducted from RT to 10 K with a step of 10–25 K. As temperature becomes lower, the temperature step is set as 10 K to have a denser data collection. For S3, the cryogenic TET characterizations are repeated for three rounds to study the structure stability and any thermal-cycling induced structure change. They are indexed as S3_r1, S3_r2 and S3_r3.

Annealing is a high temperature treatment that alters the microstructure of materials which also helps improve the thermal

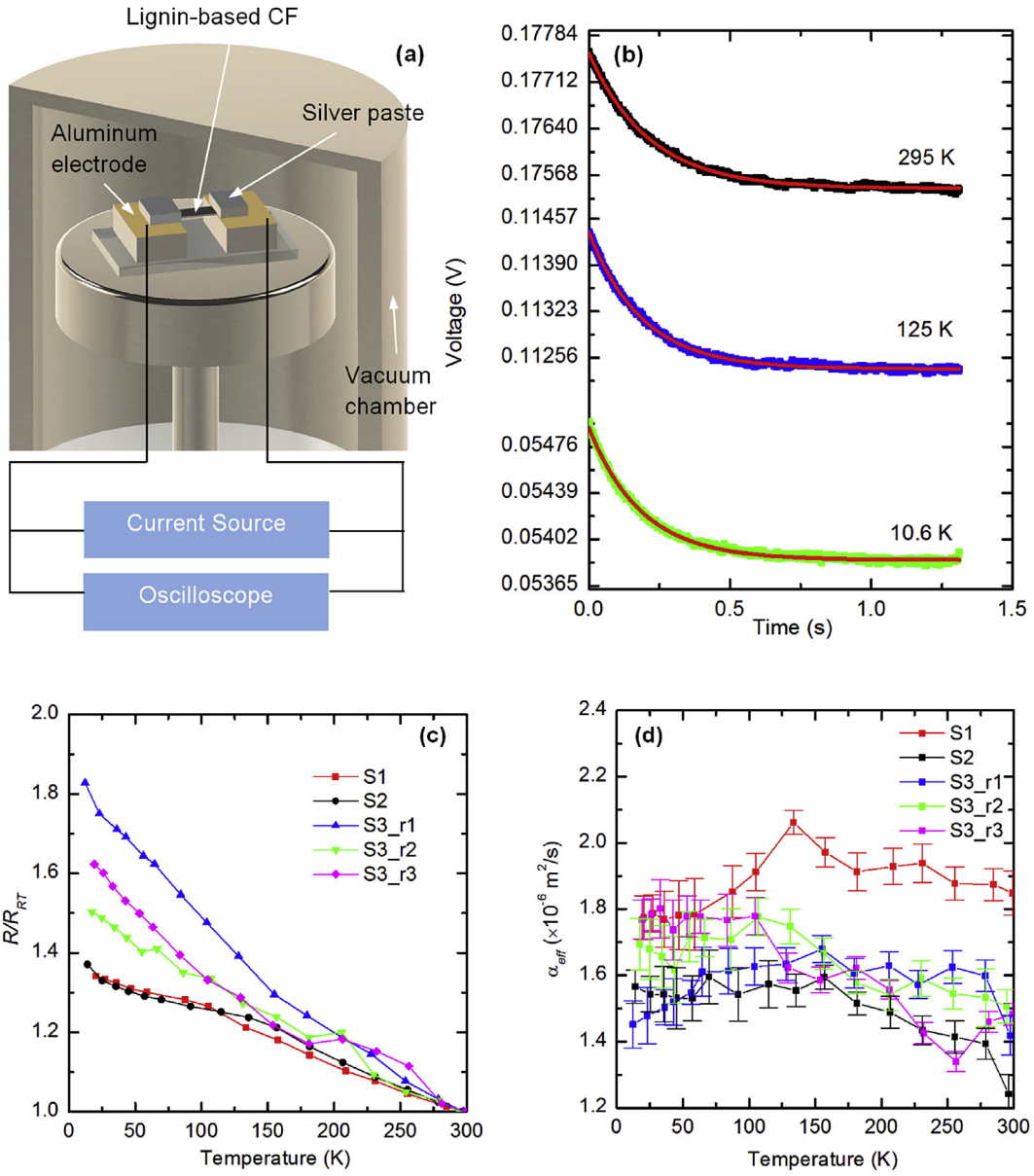

Fig. 3. **(a)** Experiment setup for the cryogenic TET technique. **(b)** The voltage profiles for S3_r1 at different temperatures: 295, 125 and 11.6 K respectively. The symbols are the experiment data and the lines are the fitting curves. **(c)** Temperature dependence of the normalized electrical resistance for three samples from RT to 10 K. **(d)** Effective thermal diffusivity of three samples. Standard deviation of the effective thermal diffusivity is also shown in the figure. (A colour version of this figure can be viewed online.)

properties. During the annealing process, the sample is placed in a vacuum chamber which is kept high vacuum (below 0.5 mTorr). In this work, a DC current offered by a current source (Keithley 6221) is fed through the sample to induce joule heating, which finally leads to high temperatures in the sample. S6 and S7 are tested to study the annealing effect on the averaged thermal properties of CFs. First, the temperature dependence of thermal properties for S6 and S7 are obtained by the cryogenic TET technique. Second, S6 and S7 are annealed only once with the annealing currents of 48 and 46 mA, respectively. After the annealing process, the thermal properties of S6 and S7 from RT down to 10 K are obtained by using the TET technique. Note that S6 and S7 are annealed only once with mediate currents. Our extensive experiments show that higher current-annealed samples are more subject to the thermally-induced breaking during cryogenic TET measurements. Furthermore, we investigate to what extent the structure and thermal properties could be improved after heavy annealing. S4 and S5 are annealed many times with increased annealing currents until the samples broke. After each annealing process, the in-situ resistance of the sample is measured by a digital multimeter. Then the in-situ thermal diffusivity of the sample is measured by the TET technique at room temperature. The average resistance (R_a) during the annealing period is obtained through dividing voltage by annealing current. With current I_a fed into the sample, the annealing power is estimated as $I_a^2 R_a$. The diameter, length and index for the seven studied CF samples are summarized in Table 2.

4. Results and discussion

4.1. Thermal transport and properties: correlation with temperature

Fig. 3(c) shows the temperature dependence of the normalized

Table 2
Details of lignin-based CFs measured in this work.

Sample Index	Diameter (μm)	Length (mm)
S1	37.97	2.07
S2	43.87	1.24
S3	40.0	1.77
S4	35.72	1.16
S5	36.10	0.905
S6	46.2	1.55
S7	43.56	1.02

electrical resistance for S1, S2 and S3. The normalized resistance is obtained by using the electrical resistance at RT as the base. Note that all samples exhibit similar nonmetallic-like behavior throughout the entire temperature range. When temperature is changed from RT to 10 K, the normalized electrical resistances are increased by 34%, 37% and 83% for S1, S2 and S3_r1, respectively. The resistance rise as temperature decreases is attributed to two factors. One is the intrinsic resistance change caused by temperature change, and the other one is the strain built in the sample as temperature decreases. The CF has a negative intrinsic resistance temperature coefficient (RTC), which means that the resistance of the CFs will increase as temperature decreases. Besides, due to the existence of functional groups in GO, graphite and GO have different thermal expansion coefficient (TEC) when temperature is lower than 300 K. Since seldom work has been published about the TEC of GO, the difference between TEC of graphene and graphene oxide is used to approximate the difference between TEC of graphite and GO. As temperature decreases from 300 to 150 K, the TEC of graphene decreases from -2.5×10^{-6} to -12.5×10^{-6} K^{-1}. The TEC of graphene remains negative when temperature is lower than 300 K. For graphene oxide paper, the TEC decreases from 9.1×10^{-5} to 0 K^{-1} as temperature decreases from 300 to ~245 K, and then the TEC (around -4.8×10^{-5} K^{-1}) changes little as temperature decreases from ~220 to ~120 K [33,34]. It is concluded that graphene oxide paper shrinks at first and then expands while graphene keeps expanding when temperature decreases from 300 to 0 K. Both graphene and graphene oxide expand as temperature decreases from 220 to 120 K. However, they expand at different rate. Analogously, we speculate that there is a thermal expansion difference between graphite and graphite oxide as temperature decreases from 300 to 0 K. Because of this, compressive strain is built up in the CF. This leads to the resistance increase when temperature is reduced. This phenomenon has been observed and discussed in our past work [35,36]. For S3, the resistance measured at three rounds show little repeatability. It has been observed that the structure change due to compressive strain could lead to permanent structure change in the material. This results in different resistance change for S3 during the three rounds measurement, even though the whole $R \sim T$ trends are similar.

During TET characterization, a small DC current (I) is fed through the CF sample to induce joule heating. With the initial resistance (R_0), steady state resistance (R_∞), and R-T relationship, we can calculate the temperature rise as $(R_\infty - R_0)/(dR/dT)$. During each TET test, the initial temperature T_0 is known, thus we got the temperature at steady state T_∞ as: $T_\infty = T_0 + (R_\infty - R_0)/(dR/dT)$. The characteristic temperature of the sample is set as the average temperature of initial and steady state temperature for the reported thermal properties. This explains why the sample temperature is a little bit higher than the environmental temperature. Fig. 3(b) shows typical TET $V \sim t$ profiles of S3_r1 when experimental temperatures are 295, 125 and 10.6 K, respectively. As temperature decreases from RT down to 10.6 K, the characteristic time changes a little. This is consistent with the fact that the measured effective thermal diffusivity varies very little as temperature decreases. The effective thermal diffusivities for three samples are shown in Fig. 3(d). It is observed that the effective thermal diffusivities change little throughout the entire temperature range. For S3_r1, the maximum and minimum effective thermal diffusivity are 1.68×10^{-6} and 1.42×10^{-6} m^2/s, respectively. The ratio of maximum to minimum value is 1.18. Besides, the effective thermal diffusivities non-monotonically change with decreased temperature. For typical polymers and graphene-based materials, the thermal diffusivity increases significantly and monotonically when temperature is decreased from RT to 10 K. For polyethylene, the ratio of maximum to minimum thermal diffusivity could be 1.8 when temperature is in the range of 10 K to RT [27,37]. This is due to fact that the thermal transport is dominated by phonon-phonon scattering in the measured sample. However, for the CFs used in this work, the thermal diffusivity changes little, indicating that the phonon scattering in CFs is dominated by the phonon-boundary scattering. The phonon scattering mechanism will be introduced in detail in section 4.2. When considering the relative error of α_{eff}, the parameter fitting error of nonlinear fitting is calculated out and it is between 0.1% and 0.3%, which is negligible. During the TET characterization, thermal diffusivity measurements of the sample under each temperature are repeated 30 to 40 times. The standard deviation due to measurement is calculated out by the repeated experimental results. Based on uncertainty propagation, the relative errors of effective thermal diffusivity are shown in Fig. 3(d).

We get the specific heat from RT down to 10 K from literature data to subtract the radiation effect [38]. Based on Eq. (3), the thermal diffusivity due to radiation is calculated out. Its magnitude is two orders of magnitude smaller than the effective thermal diffusivity. After knowing real thermal diffusivity, the real thermal conductivity (k_{real}) is obtained as $k_{real} = \alpha_{real} \cdot \rho c_p$. Fig. 4(a) shows the thermal conductivity of the samples from RT down to 10 K. Error bars are given in Fig. 4(a), too. k is determined to be 1.83–2.63 W/m·K at RT for all the samples. Considering the difference among samples, the thermal conductivities of the as-prepared samples show good consistency with each other. For comparison, the thermal conductivity of bulk amorphous carbon is also shown in Fig. 4(a) [39]. Our results are close to the reference values.

4.2. The underlying mechanism and structure-dependent phonon scattering

XRD pattern of the as-prepared CFs shows that the samples are almost amorphous. Thermal transport inside the CFs is dominated by the phonon scattering. As the sample length (L) is much longer than the phonon mean free path (Λ), the thermal transport is called diffusive transport. Under this situation, various scattering mechanism jointly determine the phonon thermal conductivity. The phonons are scattered not only by other phonons but also by grain boundary and defects. Based on the single relaxation time approximation, the phonon relaxation time (τ) could be written as: $\tau^{-1} = \tau_U^{-1} + \tau_b^{-1} + \tau_d^{-1}$. Here τ_U, τ_b and τ_d are the phonon relaxation time due to Umklapp process, phonon-boundary scattering and phonon-defect scattering, respectively. The thermal conductivity is expressed as $k = 1/3 C_p v \Lambda$, among which C_p is specific heat, v is the phonon group velocity. Λ is related with the relaxation time and can be expressed as $\Lambda = v\tau$. The thermal conductivity variation against temperature contains information about both phonon scattering and specific heat. Since specific heat is temperature dependent, it is difficult to use the thermal conductivity to directly obtain the phonon scattering information. The structure of the CFs is difficult to derive from thermal conductivity profile.

It is known that thermal diffusivity and thermal conductivity could be expressed as: $k = \rho c_p \alpha$. To get rid of the effect of heat

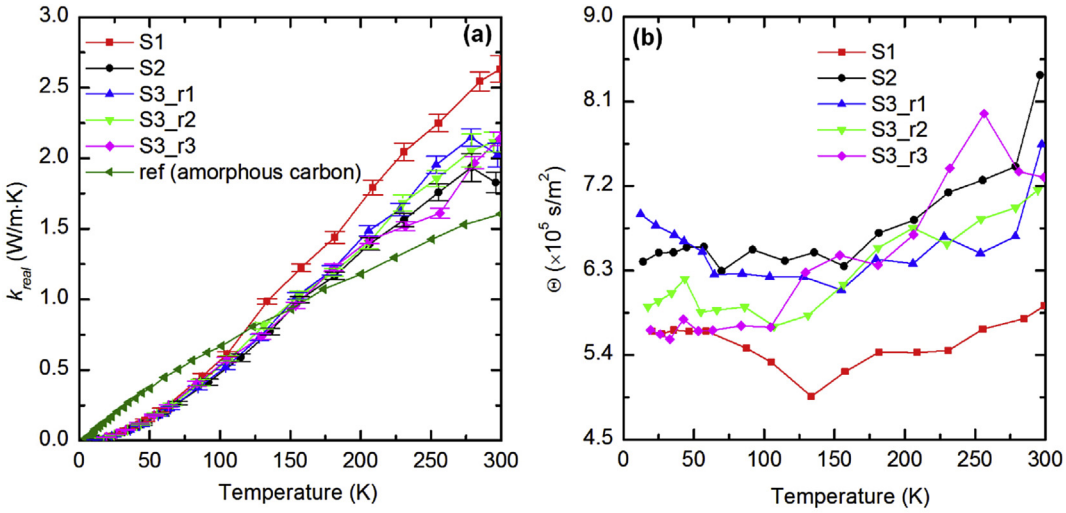

Fig. 4. **(a)** Temperature dependence of thermal conductivities for three samples. Error bars are shown in the figure. **(b)** Temperature dependence of thermal reffusivities for three samples. (A colour version of this figure can be viewed online.)

capacity, a good method is to study the thermal diffusivity only. In this section, the thermal reffusivity (Θ) is introduced and used to uncover the structure and phonon scattering in CFs. It is defined as the inverse of thermal diffusivity: $\Theta = \alpha^{-1}$. Based on the definition, Θ could be expressed as $\Theta = 3/(v\Lambda) = 3/(v^2\tau)$. Furthermore, Θ could be written as a function of phonon relaxation time due to different phonon scattering processes:

$$\Theta = 3\Big/v^2\cdot(\tau_U^{-1}+\tau_b^{-1}+\tau_d^{-1}) = 3/v\cdot(\Lambda_U^{-1}+\Lambda_b^{-1}+\Lambda_d^{-1}) = \Theta_U+\Theta_b+\Theta_d. \quad (4)$$

v changes little with temperature, but it is strongly dependent on phonon branch and phonon frequency. τ_U is strongly dependent on temperature, while τ_b and τ_d are only related with the internal micro-structure. As temperature goes down to 0 K, τ_U is approaching zero due to the quick freezing-out of phonons, while τ_b and τ_d remain almost unchanged. Thus, when temperature is 0 K, Θ_U goes to zero and the thermal reffusivity is left with Θ_b and Θ_d. It is a nonzero value at 0 K, which is caused by the grain boundaries and defects. When the phonon-boundary and phonon-defect scattering are dominant, Θ scales with the mean free path determined by boundary and defects, and it shows little temperature dependence. As the Umklapp process is dominant, Θ is strongly temperature dependent.

The thermal reffusivity variations against temperature for the three samples are shown in Fig. 4(b). It is observed that the thermal reffusivity shows very weak temperature dependence. The ratio of maximum to minimum thermal reffusivity is 1.43, indicating that phonons in the CFs are mainly scattered by grain boundaries and defects. As temperature goes down to 0 K, the estimated residual thermal reffusivity (Θ_0) are 5.67×10^5, 6.39×10^5 and 5.92×10^5 s/m^2 for S1, S2 and S3 respectively. With the knowledge of phonon velocity and residual thermal reffusivity, Λ_{eff} could be calculated as $\Lambda_{eff} = 3/(\Theta_0 v)$. The phonon velocity can be determined from the dispersion relation: $\partial\omega/\partial\kappa$. ω and κ are the angular frequency and wavenumber. In this work, phonon velocity is estimated as 4300 m/s, which is taken from the phonon velocity in pyrolytic graphite [40,41]. Thus, Λ_{eff} are determined to be 1.23, 1.1 and 1.18 nm for the three samples, respectively. The calculated Λ_{eff} is limited by the phonon-grain boundary/defect scattering in all directions. In the former part, the relationship between thermal conductivity and mean free path was introduced: $k = 1/3C_p v\Lambda_{eff}$. The k is proportional to mean free path. A longer mean free path could lead to a larger thermal conductivity.

Table 3 summarizes the crystallite size measured by XRD and cluster size obtained by Raman method, as well as the mean free path uncovered by phonon-boundary/defect scattering. Since a bundle of CF samples were tested in the crystallite size measurement by XRD, the obtained crystallite size is reasonable to be the averaged crystallite size of each CF. S4 and S5 broke when the annealing temperature reached a certain value, so we could not get Λ_{eff} of S4 and S5. It is found that L_a measured by Raman, L_c obtained by XRD and Λ_{eff} show the same order of magnitude. However, the mechanisms of the three kinds of size are different. L_a obtained by Raman is induced by optical phonon scattering, and it indicates the mean free path of optical phonons. Since the thermal transport is dominated by the scattering of acoustic phonons, Λ_{eff} is determined by acoustic phonon scattering. The phonon scattering mechanisms of optical phonon and acoustic phonon can be quite different. This is the reason for the discrepancy between L_a and Λ_{eff}. As we mentioned before, the crystallite size along the edge and basal plane is 0.9 and 1.3 nm, respectively. The crystallite sizes measured by XRD are different in different crystallite orientations. Λ_{eff} indicates the effective phonon mean free path due to grain boundaries and defects. This leads to the discrepancy between the crystallite size and Λ_{eff}. For the material whose crystallite size is difficult to obtain by XRD, the thermal reffusivity mechanism offers an alternative method to estimate the order of crystallite size and study the corresponding acoustic phonon mean free path due to grain boundaries and defects.

Table 3
Crystallite size measured by XRD, cluster size obtained by Raman method and mean free path due to phonon-boundary/defect scattering.

	L_c by XRD [(100) direction] (nm)	L_c by XRD [(002) direction] (nm)	L_a by Raman (nm)	Λ_{eff} (nm)
S1	1.3	0.9	2.31	1.23
S2				1.1
S3				1.18

5. Annealing effect on structure and thermal transport

5.1. Change of structure domain size by annealing

In this section, two samples (S6 and S7) were chosen to conduct annealing and study the thermo-physical properties over the cryogenic temperature range. We aim at gaining full understanding of the annealing effect on effective thermal conductivity and phonon mean free path. After obtaining the temperature dependence of thermal diffusivity by the TET technique, the real thermal conductivity is obtained by the following equation: $k = \rho c_p \alpha$. Fig. 5(a) shows the temperature dependence of thermal conductivity for the pre-annealed and post-annealed samples. It could be observed that the k of S6 and S7 at RT increases by 44% and 24% by annealing. The different annealing level leads to the discrepancy of thermal property improvement between S6 and S7.

To better understand the micro-structure improvement by annealing, the thermal reffusivity of the two samples are evaluated. The thermal reffusivity has been introduced in section 4.2, and it could be used to determine the effective phonon mean free path. Fig. 5(b) shows the temperature dependence of the thermal reffusivity for S6 and S7. During the whole cryogenic temperature range, with the same measurement temperature, the thermal reffusivity decrease by annealing is in the range of: 2×10^5–3×10^5 s/m^2 for S6 and 1.2×10^5–2×10^5 s/m^2 for S7. The residual thermal reffusivity for pre-annealed and post-annealed S6 is determined to be 7.13×10^5 and 4.11×10^5 s/m^2. The residual thermal reffusivity for pre-annealed and post-annealed S7 is determined to be 8.10×10^5 and 6.31×10^5 s/m^2. With known residual thermal reffusivity, the effective mean free path is determined according to the following equation: $\Lambda_{eff} = 3/(\Theta_0 v)$, and it is summarized in Table 4. The effective mean free paths of S6 and S7 are increased by 72% and 28% after annealing. It is known that phonon scattering is limited by the grain boundary/defect at almost 0 K. A longer effective mean free path indicates that the increase of grain size and less defects in annealed samples. Table 4 also summarizes the resistance, thermal conductivity/diffusivity at RT, and residual thermal reffusivity for pre-annealed and post-annealed samples.

Here, one point about the measured thermal properties and effective mean free path should be explained. The thermal transport during annealing process is a 1-D problem, which means the temperature distribution along the fiber axial direction is not uniform. Under this situation, different parts of the sample are annealed at different levels. The region close to the two ends receives almost no annealing. In this section, the thermal properties and effective mean free path are the averaged properties of the materials, which cannot reflect the very localized structure and localized thermal conductivity change by annealing. Besides, we have found that the sample could not sustain the cycle of cryogenic temperature measurement when the annealing current is too high. In the next section, we focus on S4 and S5 and increase the annealing currents until they broke. The thermal conductivity at the middle point and the local temperature are determined to give the precise information on thermal conductivity increase under different annealing temperatures. Also, Raman spectra are obtained at different locations of the sample to track the change of the structure due to different annealing levels.

5.2. Transient material behavior during annealing

The samples denoted as S4 and S5 were subjected to the annealing treatment. The original resistances of S4 and S5 are 138.0 and 67.9 Ω, respectively. For S4, the annealing current increases from 16 to 107 mA with a multiplication factor in the range

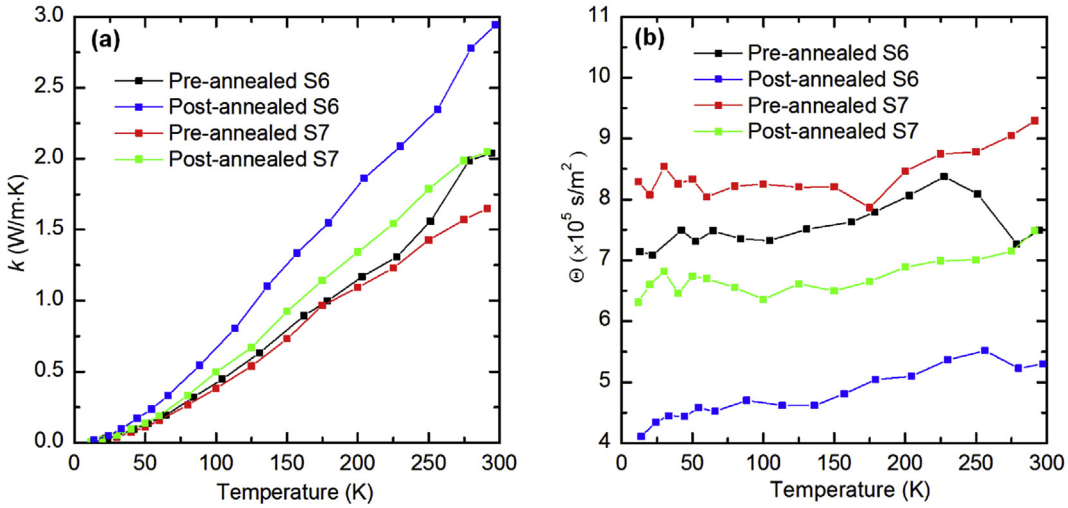

Fig. 5. **(a)** Temperature dependence of thermal conductivity for pre-annealed and post-annealed samples. **(b)** Temperature dependence of thermal reffusivity for pre-annealed and post-annealed samples. (A colour version of this figure can be viewed online.)

Table 4
Summarization of resistance, thermal conductivity/diffusivity at RT, and residual thermal diffusivity and effective mean free path for S6 and S7.

		R (Ω)	k (W/m·K)	α (m^2/s)	Θ_0 (s/m^2)	Λ_{eff} (nm)
S6	Pre-annealed	136	2.0	1.36×10^{-6}	7.13×10^5	0.90
	Post-annealed	67.7	2.9	1.88×10^{-6}	4.11×10^5	1.55
S7	Pre-annealed	149.4	1.65	1.07×10^{-6}	8.10×10^5	0.79
	Post-annealed	104.4	2.0	1.34×10^{-6}	6.31×10^5	1.01

1.05–1.1. For S5, the annealing current increases from 3 to 206 mA with a multiplication factor in the range 1.05–1.1. The annealing time lasts from 30 to 70 s. The voltage evolution of the sample during annealing is monitored by an oscilloscope (DPO 3052), through which the resistance during annealing process can be derived.

Fig. 6(a) and (b) show the voltage evolutions with different annealing currents for S4 and S5. The voltage evolution consists of two states. In state 1, the voltage of the sample drops very quickly upon the annealing current. In this state, there is very little annealing, and joule heating process dominates. It is like the TET heating and resistance changing process. Since the carbon fiber shows a negative temperature-resistance coefficient, the high temperature caused by the joule heating leads to a very quick resistance decrease. This finally results in the quick voltage drop. It is observed that state 1 becomes shorter as annealing current increases. This is consistent with the fact that the structure of the CF improves after annealing. Better structure leads to a higher thermal diffusivity, so that the characteristic time becomes shorter with the increased annealing current. State 2 is the annealing process. During this process, high temperature annealing helps reduce the internal stress and eliminate lattice vacancies in the samples, thus the resistance decreases with a very slow rate. When the annealing current is 16 mA for S4 and 6.4 mA for S5, the voltage of the samples shows negligible change in state 2. This indicates that when the annealing current is small, the temperature in the sample is not high enough to induce annealing. Only as temperature increases to a certain value, the annealing process starts. In section 5.3, we will introduce the resistance variation with annealing power, the localized structure and thermal properties increase of S4 and S5 in detail.

5.3. Change of structure and thermal conductivity under annealing until broke

The resistance variations with increased annealing power for S4 and S5 are shown in Fig. 7(a). The annealing temperature has a positive correlation with the annealing power. Therefore, the annealing power could be used to indicate the annealing temperature of the sample. At first, the resistance decreases at a higher rate. As annealing power becomes larger, the resistance saturates and then it increases a little bit. Finally, the sample broke at the middle point. Since the midpoint has the highest temperature during annealing, the breakage could be attributed to structural shrinkage of CF under elevated temperatures. The annealing current when the sample broke is defined as maximum current (I_m). The electrical resistance of the two samples decreased by around 40% after being completely annealed. Fig. 7(b) shows the broken sample (S4) under SEM. During the annealing process, the microstructure of graphite improves and fraction of graphite increases. This will be studied by Raman spectroscopy later. Besides, the functional groups in the CFs reduce. These two factors explain the electrical conductivity increase after annealing. This speculation in structure change is further detailed and supported in the following Raman study.

We conducted Raman spectrum study of S4 after broke at different locations from the broken point to the electrode end. Since the temperature distribution during annealing is not uniform, we used the measured thermal diffusivity and the derived thermal conductivity to estimate the temperature at different locations that corresponding to the measured Raman spectrum. l_d is defined as the distance of measured point to the broken point and its definition schematic is shown in Fig. 7(b). Fig. 7(d) shows the temperature distribution along the fiber axis under the maximum annealing current (I_m) in the sample. The original point of the x-axis

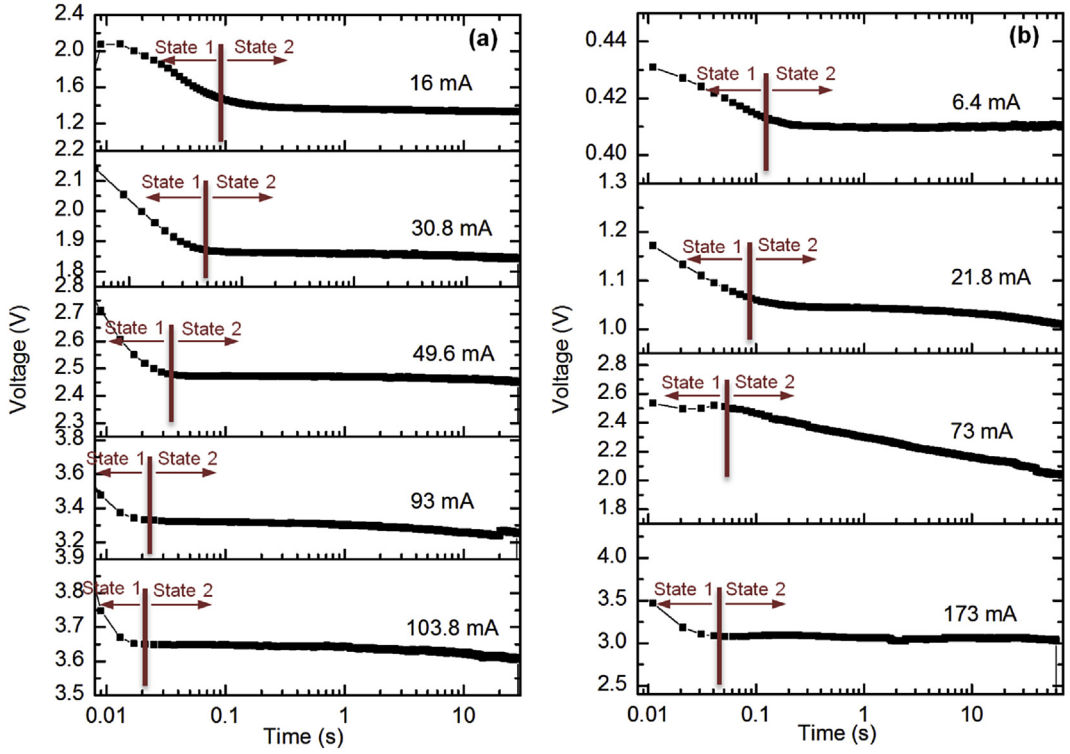

Fig. 6. Voltage evolutions to show the two states during annealing process under different annealing currents for **(a)** S4 and **(b)** S5. (A colour version of this figure can be viewed online.)

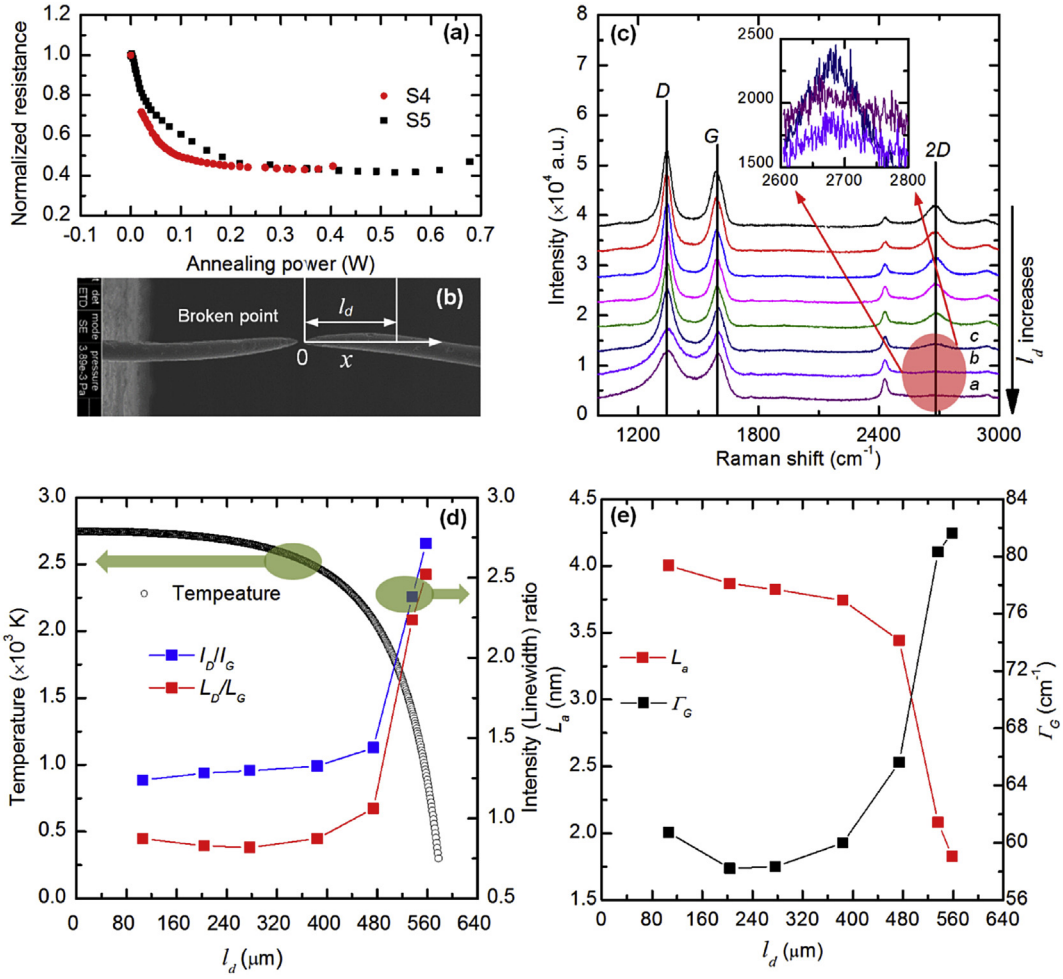

Fig. 7. **(a)** Annealing power dependence of electrical resistance for S4 and S5. **(b)** S4 under SEM after breaking. The definition of l_d is also shown in the figure. **(c)** Raman spectrum at different points of S4. It is observed that the *D* and *G* peak become sharper when the tested point is closer to broken point. The inset shows a clear view of the 2*D* peak of point *a*, *b* and *c*. Point *a*, *b* and *c* are very close to the electrode end. **(d)** S4: Intensity ratio of *D* peak (I_D) to *G* peak (I_G) changes with l_d; Linewidth ratio of *D* peak (L_D) to *G* peak (L_G) changes with l_d. The data shown in open circles gives the simulation result of temperature distribution before the sample broke. **(e)** Cluster size obtained by Raman (L_a) and linewidth of *G* peak (Γ_G) as a function of l_d. (A colour version of this figure can be viewed online.)

is the broken point of the sample. As l_d increases, the temperature of the sample decreases. Our Raman study gave the information on how the structure of the annealed CF changes along the fiber axial direction.

Raman spectra of S4 measured at 532 nm excitation are given in Fig. 7(c). The lens and integration time is 20× and 5 s, respectively. The inset of Fig. 7(c) gives a clear view of spectrum for point *a*, *b* and *c*. Point *a*, *b* and *c* are very close to the electrode end. From Fig. 7(c), very wide and small 2*D* peak is found as the tested point is close to the electrode end. Also, *D* peak and *G* peak are wide and overlap for the tested point close to the electrode end. It shows a representative Raman spectrum of disordered GO [21]. As the tested points are closer to the broken point (l_d becomes smaller), a single 2*D* peak at 2677 cm^{-1} starts to emerge. The Gaussian function is used to fit the 2*D* peak. Its full width at half maximum (FWHM) is ~92 cm^{-1}, which is four-fold larger than that of 2*D* peak for graphene [21]. At the same time, both *D* peak and *G* peak become sharper as the tested point becomes closer to the broken point. Based on these results, we can conclude that the structure of graphite becomes better and the graphite concentration becomes higher in the annealed CF.

To further estimate the cluster size change by annealing, two-peak Lorentz function is used to fit the *D* and *G* peak to obtain the intensity and linewidth (Γ_D and Γ_G). Fig. 7(d) shows the value of I_D/I_G and Γ_D/Γ_G changing with l_d. As l_d decreases from 558 to 106 μm (from strongly annealed region to less annealed region), I_D/I_G decreases from 2.71 to 1.11, indicating that annealing the CFs with higher temperatures improves the structure order. As we mentioned before, the cluster size (L_a) has the following relationship with I_D/I_G: $I_D/I_G = C(\lambda)/L_a$. Thus, the cluster size is calculated and its variation with l_d is shown in Fig. 7(e). It is observed that L_a decreases from 4 to 1.83 nm as l_d increases from 60.7 to 557.9 μm. Fig. 7(e) also shows the Raman spectrum linewidth of *G* peak (Γ_G) changing with l_d. The optical phonon lifetime (τ) has the following relationship with Γ_G: $\tau^{-1} = 2c\pi\Gamma_G$. c (=3 × 10^8 m/sec) is the speed of light [42]. Γ_G increases with the increased l_d, indicating that optical phonon lifetime decreases with increased l_d. This strongly supports the conclusion that annealing significantly improves the structure order, which can be reflected by a longer optical phonon lifetime. The annealing effect on the structure of the sample is strongly dependent on the annealing temperature. The middle part of the sample has a higher annealing temperature, leading to a better structure of the middle part. On the other hand, the temperature of the sample close to the electrode is much smaller, resulting in almost no annealing effect.

In the annealing process, after each annealing, the thermal

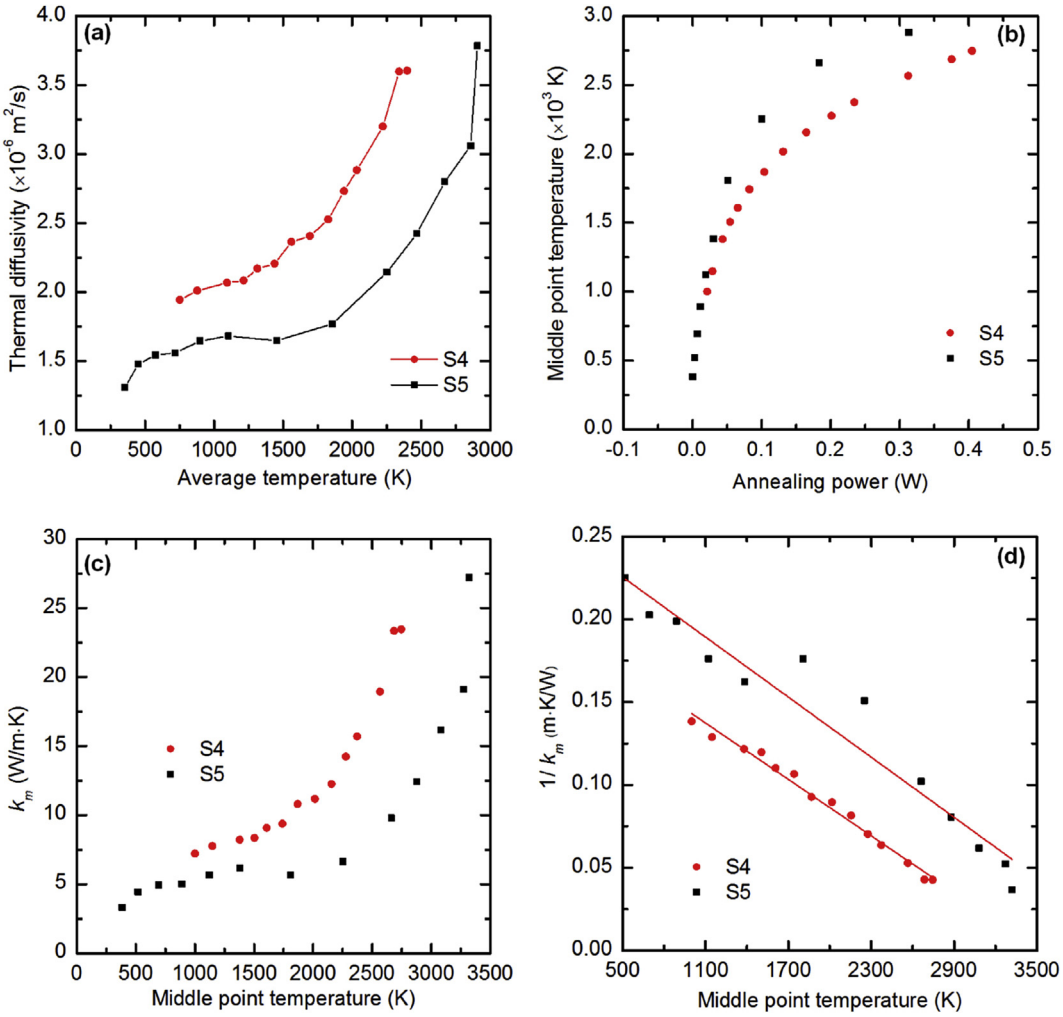

Fig. 8. **(a)** Thermal diffusivity of the sample changes with average temperature (T_a) during the annealing process. **(b)** Temperature variations of middle point against annealing power during annealing. **(c)** Thermal conductivity of middle point changes with temperature of middle point. **(d)** Inverse of thermal conductivity of middle point ($1/k_m$) changes with temperature of middle point (T_m). (A colour version of this figure can be viewed online.)

conductivity of the sample is measured using the TET technique. But this scenario is different from the measurement of as-synthesized sample. For the as-synthesized sample, the thermal conductivity and diffusivity are uniform along the sample. But for the annealed sample, due to the nonuniform temperature distribution along the fiber axial direction in annealing, the whole sample is not annealed at the same level. Therefore, the thermal conductivity along the fiber axial direction will vary. In our TET data processing, this non-uniform k effect is considered using numerical modeling. In the 1D numerical thermal transport simulation, the thermal conductivity along the fiber axis direction is assumed to be linearly distributed. Since the temperatures at the two electrodes change very little during the annealing process, the k at two ends is set as the thermal conductivity of as-prepared samples. The middle point of the sample has the highest annealing temperature, leading to a maximum k at the middle point. We used 1D numerical thermal transport simulation based on the finite difference method to simulate the temperature evolution for TET data processing. During the simulation process, the emissivity is set as 0.85, which is the same value used in calculating out the effect of radiation on thermal diffusivity before. k of as-prepared samples takes 1.75 W/m·K. By varying the k at middle point, we get multiple normalized temperature evolutions changing with time. The one best fitting the experimental result is taken as the property of the sample. This middle point thermal conductivity is termed as k_m.

To evaluate the temperature of the middle point (T_m) and the average temperature (T_a) during annealing, the above obtained k_m is used to model the steady-state heat conduction in S4 and S5 during annealing. In the steady-state heating model, the emissivity of CF is set as 0.85 at RT. As annealing power increases, the temperature of the sample increases as well. The emissivity of CF deviates from 0.85 when temperature is high. We found that when emissivity changes with ±10%, the obtained T_m shows a 2% variation. Thus, we set the emissivity of CF as 0.85 in the temperature range 300–2800 K. Fig. 8(a) shows the measured real thermal diffusivity (α_{real}) variation with the average temperature during the annealing process. When the average temperature increases from 700 to 2300 K, α_{real} increases by 80% and 150% for S4 and S5, respectively. Fig. 8(b) shows how T_m changes with annealing power in the sample. As the annealing power increases, the temperature at the middle point reaches to a certain value, under which the sample broke. This temperature is termed T_c. T_c is determined to be ~2800 K. It is reported that the melting point of graphite is 4489 °C under 10.3 MPa [32]. T_c of CFs is much smaller than the melting point of graphite, indicating the intrinsic defective graphite structure. Fig. 8(c) shows the k_m change with annealing temperature at

the middle point. Overall, k_m increases monotonically with the annealing temperature. As temperature in the range of 800–2000 K, k_m increases at a slower rate. It increases from 7.2 to 11.2 W/m·K, by 55.6%. As annealing temperature is above 2000 K, k_m increases faster. It is increased by 110%, from 11.2 to 23.5 W/m·K. It is concluded that when the annealing temperature becomes higher, the fiber is annealed more heavily, leading to much more improved microstructure. This has also been confirmed by Raman study before. Fig. 8(d) shows the inverse of k_m as a function of annealing temperature. A linear fitting between the inverse of k_m and midpoint temperature is obtained and shown in the figure. The correlation between $1/k_m$ and T_m is obtained as $1/k_m = 0.1997-5.669 \times 10^{-5}T_m$ for S4. This correlation offers us a quick method to predict the annealed thermal conductivity with known annealing temperatures.

6. Conclusion

In this work, the micro-structure and thermo-physical properties of lignin-based microscale CFs were studied from various aspects. Our thermal measurement indicated that the thermal conductivity of the lignin-based CFs could be as small as 1.83 W/m·K. Our thermal reffusivity study from RT down to 10 K showed very weak variation of thermal reffusivity against temperature. This phenomenon suggested dominant boundary/defect phonon scattering-sustained heat conduction in our CFs. By utilizing a new parameter: thermal reffusivity, the mean free path of phonon scattering due to grain boundary and defects in the lignin-based CFs was determined. This value (~1.2 nm) agrees well with the structure domain size determined by XRD (0.9 and 1.3 nm) and Raman spectroscopy (2.31 nm). The annealing effects on microstructure and thermal conductivity were studied by micro-Raman spectroscopy and simulation. The as-prepared CFs only showed a typical structure of graphite oxide. After being highly annealed, the concentration of graphite in the annealed CFs increased and the microstructure of graphite improved. The average thermal conductivity of annealed lignin-based CFs could be increased by 24%–44% at RT. Significant increase of the effective phonon mean free path could be obtained by annealing. The localized thermal conductivity of annealed lignin-based CFs could be increased by ten fold to as high as ~24 W/m·K. The structure improvement was also studied by micro-Raman scanning from the highly-annealed region to weakly-annealed region, showing a one-fold increase in the cluster size by annealing. The inverse of thermal conductivity was found to have a linear relationship with annealing temperature, which offers a possible way for predicting the thermal conductivity after different current annealing.

Acknowledgement

Support of this work by National Science Foundation (CBET1235852, CMMI1264399), Department of Energy (DENE0000671, DE-EE0007686), and Iowa Energy Center (MG-16-025, OG-17-005) is gratefully acknowledged.

References

[1] H. Mainka, O. Täger, E. Körner, Liane L. Hilfert, Sabine S. Busse, Frank F.T. Edelmann, et al., Lignin-an alternative precursor for sustainable and cost-effective automotive carbon fiber, J. Mater. Res. Technol. 4 (2015) 283–296.
[2] K. Naito, Y. Tanaka, J.M. Yang, Y. Kayawa, Tensile properties of ultrahigh strength PAN-based, ultrahigh modulus pitch-based and high ductility pitch-based carbon fibers, Carbon 46 (2) (2008) 189–195.
[3] J. Luo, Lignin-based Carbon Fiber, The University of Maine, Orono ME USA, 2010. PhD thesis.
[4] H.C. Liu, A.T. Chien, B.A. Newcomb, Y.D. Liu, S. Kumar, Processing, structure, and properties of lignin- and CNT-incorporated polyacrylonitrile-based carbon fibers, ACS Sustain. Chem. Eng. 3 (9) (2015) 1943–1954.
[5] E. Mora, C. Blanco, V. Prada, R. Santamaria, M. Granda, R. Menendez, A study of pitch-based precursors for general purpose carbon fibres, Carbon 40 (14) (2002) 2719–2725.
[6] J. Heremans, I. Rahim, M.S. Dresselhaus, Thermal conductivity and Raman spectra of carbon fibers, Phys. Rev. B 32 (10) (1985) 6742–6747.
[7] G. Gellerstedt, E. Sjoholm, I. Brodin, The wood-based biorefinery: a source of carbon fiber? Open Agric. J. 3 (2010) 119–124.
[8] A. Duval, M. Lawoko, A review on lignin-based polymeric, micro-and nano-structured materials, React. Funct. Polym. 85 (2014) 78–96.
[9] D.A. Baker, T.G. Rials, Recent advances in low-cost carbon fiber manufacture from lignin, J. Appl. Polym. Sci. 130 (2) (2013) 713–728.
[10] Q.N. Sun, R. Khunsupat, K. Akato, J.M. Tao, N. Labbe, N.C. Gallego, et al., A study of poplar organosolv lignin after melt rheology treatment as carbon fiber precursors, Green Chem. 18 (18) (2016) 5015–5024.
[11] X.Z. Dong, C.X. Lu, P.C. Zhou, S.C. Zhang, L.Y. Wang, D.H. Li, Polyacrylonitrile/lignin sulfonate blend fiber for low-cost carbon fiber, RSC Adv. 5 (53) (2015) 42259–42265.
[12] D.A. Baker, T.G. Rials, Recent advances in low-cost carbon fiber manufacture from lignin, J. Appl. Polym. Sci. 130 (2) (2013) 713–728.
[13] F.S. Baker, N.C. Gallego, D.A. Baker, Low Cost Carbon Fiber from Renewable Resources, EERE, US Dept of Energy Project ID# lm_03_baker, 2010.
[14] Y. Huang, R.J. Young, Effect of fiber microstructure upon the modulus of PAN- and pitch-based carbon fibers, Carbon 33 (2) (1995) 97–107.
[15] R. Paul, D. Burwell, X. Dai, A. Naskar, N. Gallego, K. Akato, Recent Progress in Producing Lignin-based Carbon Fibers for Functional Applications, 2015. United States, http://www.osti.gov/scitech/servlets/purl/1224679.
[16] E. Mayhew, V. Prakash, Thermal conductivity of individual carbon nanofibers, Carbon 62 (2013) 493–500.
[17] K. Naito, J.M. Yang, Y.B. Xu, Y. Kagawa, Enhancing the thermal conductivity of polyacrylonitrile- and pitch-based carbon fibers by grafting carbon nanotubes on them, Carbon 48 (6) (2010) 1849–1857.
[18] W.D. Qu, Y. Xue, Y.W. Gao, M. Rover, X.L. Bai, Repolymerization of pyrolytic lignin for producing carbon fiber with improved properties, Biomass Bioenergy 95 (2016) 19–26.
[19] A. Pollard, M. Rover, R. Brown, Characterization of bio-oil recovered as stage fractions with unique chemical and physical properties, J. Anal. Appl. Pyrolysis 93 (2012) 129–138.
[20] A. Kaniyoor, S. Ramaprabhu, A Raman spectroscopic investigation of graphite oxide derived graphene, AIP Adv. 2 (3) (2012) 032183.
[21] A.C. Ferrari, Raman spectroscopy of graphene and graphite: disorder, electron-phonon coupling, doping and nonadiabatic effects, Solid State Commun. 143 (1–2) (2007) 47–57.
[22] A.C. Ferrari, J. Robertson, Interpretation of Raman spectra of disordered and amorphous carbon, Phys. Rev. B 61 (20) (2000) 14095–14107.
[23] F. Tuinstra, J.L. Koenig, Raman spectrum of graphite, J. Chem. Phys. 53 (3) (1970) 1126–1130.
[24] H.C. Schniepp, J.L. Li, M.J. McAllister, H. Sai, M. Herrera-Alonso, D.H. Adamson, et al., Functionalized single graphene sheets derived from splitting graphite oxide, J. Phys. Chem. B 110 (17) (2006) 8535–8539.
[25] B. Nysten, J.P. Issi, R. Barton, D.R. Boyington, J.G. Lavin, Determination of lattice defects in carbon fibers by means of thermal-conductivity measurements, Phys. Rev. B 44 (5) (1991) 2142–2148.
[26] L. Qiu, X.H. Zheng, J. Zhu, G.P. Su, D.W. Tang, The effect of grain size on the lattice thermal conductivity of an individual polyacrylonitrile-based carbon fiber, Carbon 51 (2013) 265–273.
[27] J. Liu, Z.L. Xu, Z. Cheng, S. Xu, X.W. Wang, Thermal conductivity of ultrahigh molecular weight polyethylene crystal: defect effect uncovered by 0 K limit phonon diffusion, ACS Appl. Mater. Interfaces 7 (49) (2015) 27279–27288.
[28] J.Q. Guo, X.W. Wang, T. Wang, Thermal characterization of microscale conductive and nonconductive wires using transient electrothermal technique, J. Appl. Phys. 101 (6) (2007) 063537.
[29] Y. Sekii, T. Hayashi, Measurements of reflectance and thermal emissivity of a black surface created by electrostatic flocking with carbon fiber Piles, IEEE Trans. Dielectr. Electr. Insul. 16 (3) (2009) 649–654.
[30] F.P. Incropera, D.P. DeWitt, Fundamentals of Heat and Mass Transfer, fifth ed., Wiley, New York, 2002.
[31] J.Q. Guo, X.W. Wang, L.J. Zhang, T. Wang, Transient thermal characterization of micro/submicroscale polyacrylonitrile wires, Appl. Phys. A Mater. Sci. Process 89 (1) (2007) 153–156.
[32] W.M. Haynes, CRC Handbook of Chemistry and Physics (Internet version), 97th ed., CRC Press/Taylor & Francis, Boca Raton, 2017.
[33] D. Yoon, Y.W. Son, H. Cheong, Negative thermal expansion coefficient of graphene measured by Raman spectroscopy, Nano Lett. 11 (8) (2011) 3227–3231.
[34] Y.J. Su, H. Wei, R.G. Gao, Z. Yang, J. Zhang, Z.H. Zhong, et al., Exceptional negative thermal expansion and viscoelastic properties of graphene oxide paper, Carbon 50 (8) (2012) 2804–2809.
[35] J. Liu, T.Y. Wang, S. Xu, P.Y. Yuan, X. Xu, X.W. Wang, Thermal conductivity of giant mono- to few-layered CVD graphene supported on an organic substrate, Nanoscale 8 (19) (2016) 10298–10309.
[36] Y.S. Xie, P.Y. Yuan, T.Y. Wang, N. Hashemi, X.W. Wang, Switch on the high thermal conductivity of graphene paper, Nanoscale 8 (40) (2016) 17581–17597.
[37] Y.S. Xie, Z.L. Xu, S. Xu, Z. Cheng, N. Hashemi, C. Deng, et al., The defect level

and ideal thermal conductivity of graphene uncovered by residual thermal reffusivity at the 0 K limit, Nanoscale 7 (22) (2015) 10101–10110.
[38] W. Desorbo, W.W. Tyler, The specific heat of graphite from 13 to 300 K, J. Chem. Phys. 21 (10) (1953) 1660–1663.
[39] A.A. Balandin, Thermal properties of graphene and nanostructured carbon materials, Nat. Mater. 10 (8) (2011) 569–581.
[40] G.A. Slack, Anisotropic thermal conductivity of pyrolytic graphite, Phys. Rev. 127 (3) (1962) 694–701.
[41] C.H. Deng, Y.M. Sun, L.J. Pan, T.Y. Wang, Y.S. Xie, J. Liu, et al., Thermal diffusivity of a single carbon nanocoil: uncovering the correlation with temperature and domain size, ACS Nano 10 (2016) 9710–9719.
[42] K.J. Thomas, M. Sheeba, V.P.N. Nampoori, C.P.G. Vallabhan, P. Radhakrishnan, Raman spectra of polymethyl methacrylate optical fibres excited by a 532 nm diode pumped solid state laser, J. Opt. A Pure Appl. Opt. 10 (5) (2008) 055303.